



Non-sorting multi-objective optimization of flexible roll forming using artificial neural networks

Yaghoub Dadgar Asl^{1,2} · Young Yun Woo² · Yangjin Kim² · Young Hoon Moon²

Received: 26 May 2019 / Accepted: 13 March 2020 / Published online: 29 March 2020
© Springer-Verlag London Ltd., part of Springer Nature 2020

Abstract

The main defects due to flexible roll forming (FRF) processes include longitudinal bow and wrinkling. In this study, experimental and numerical analyses were performed using three different blank shapes to characterize the effects of the process parameters on defects in parts fabricated by FRF with and without leveling roll. Owing to the complexity of the FRF process, two algorithms were combined for its optimization. Artificial neural network-based Non-dominated Sorting Genetic Algorithm II (NSGA-II) was used to optimize the effective parameters of the FRF process, such as the sheet thickness, yield strength, and blank shape, with respect to the target bend angle to minimize the longitudinal bow and wrinkling of the product. The back-propagation neural network (BPNN) was used to identify two objective functions, while non-sorting multi-objective algorithm simulation was used to optimize the input parameters to minimize the objective functions. The results showed that the sheet thickness had the greatest effect on the minimization of the two objective functions, followed by the yield strength and blank shape, respectively.

Keywords Flexible roll forming (FRF) · Longitudinal bow · Wrinkling · Finite element (FE) · Back-propagation neural network (BPNN) · Non-dominated sorting genetic algorithm II (NSGA-II)

1 Introduction

Roll formed parts have many applications in several industries, such as the automobile industries, ship construction, and aerospace industries, to reduce the material weight of fabricated parts without degrading their performance [1]. In conventional roll forming processes for the fabrication of parts with constant cross sections, the initial blank is converted gradually to the target profile using a series of rotary rolls, as shown in Fig. 1a. In many applications, products with variable cross sections require weight loss and performance enhancement; this weight loss is possible by using forming processes such as roll forming, flexible roller forming, and hydro-forming [2–5]. Flexible roll forming was developed to overcome the limitations of the traditional roll forming process, and several studies have been performed on shape analysis

and process-induced fracture [6, 7]. In flexible roll forming (FRF), the forming rolls have a linear and rotational motion on the bend line to produce the desired profile with the variable cross section, as illustrated in Fig. 1b.

Shape defects may occur owing to complex deformation in FRF. In general, non-uniform elongations of the material and the related non-homogeneous deformations over the thickness or width of the blank may result in waviness or curvatures. One of the major defects caused by FRF is longitudinal bow, which is the creation of a height deviation at the profile web in the longitudinal direction. The cause of the bow is the non-homogeneous distribution of the longitudinal strain or non-uniform elongation of the blank, as shown in Fig. 2a and b [8].

Another major defect caused by FRF is wrinkling, which is instable deformation owing to increase the compression at the longitudinal direction of the flange. This is due to the complex deformations that occur in an area where there is a change in cross section, resulting in some portions of the flange being compressed in the longitudinal direction of the profile [9]. The occurrence of wrinkling during a FRF process is illustrated in Fig. 3a and b.

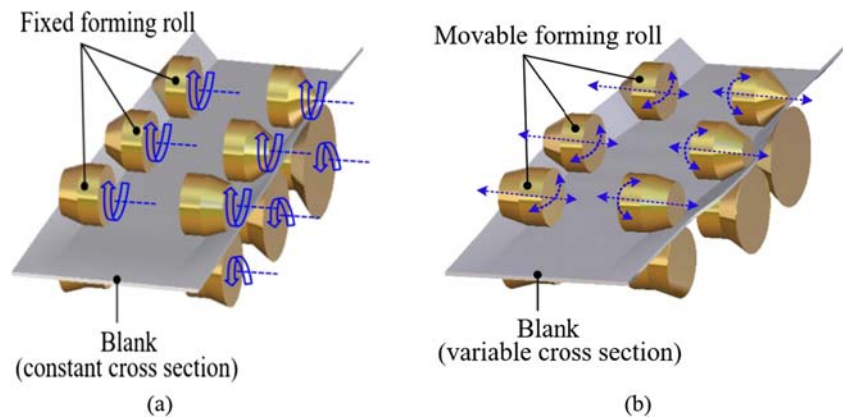
Most previous studies on traditional roll forming and FRF focused on investigating process parameters, the causes of defects in the product, and the effects of the process

✉ Young Hoon Moon
yhmoon@pusan.ac.kr

¹ Department of Mechanical Engineering, Tehran Branch, Technical and Vocational University, Tehran, Iran

² School of Mechanical Engineering, Pusan National University, 30 Jangjeon-dong, Geumjeong-gu, Busan 46241, Republic of Korea

Fig. 1 **a** Traditional roll forming process. **b** Flexible roll forming



parameters on the occurrence of defects. Farzin et al. [10] presented the buckling limit of strain (BLS) as an important factor of the roll forming process. Their results showed that a product has no edge buckling when the longitudinal strain remaining in the longitudinal direction is 0, and the buckling rate is independent from the value of bend angle and is a function of the sheet material properties and the ratio of thickness to flange length. Salmani Tehrani et al. [11] analyzed the localized edge buckling in the cold roll forming process. They resulted that the cause of this defect is the development of the longitudinal strain in the process, reducing the local tensile strength, and increasing the compressive deformation. Gulceken et al. [12] simulated the FRF process using the finite element software MSC Marc. The roll design to produce the profiles with variable cross section in FRF was characterized. Larenga and Galdos [13] used local heating during FRF to reduce web warping. Kasaei et al. [9] used finite element analysis to investigate wrinkling in flange of the profile. According to the results of the study, wrinkling occurs when the longitudinal compressive strain is less than the compressive strain required to obtain the target geometry in the transition zone as calculated by mathematical modeling. Mohammadi et al. [14] used finite element simulation to examine the occurrence of web warping. The results showed that the main cause of this defect was insufficient strain at the edge of the wings of the profile in the transition zone.

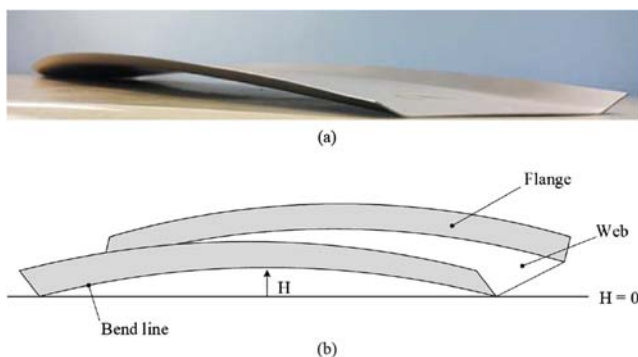


Fig. 2 Longitudinal bow caused by flexible roll forming: **a** photograph and **b** schematic illustration

Jiao et al. [15] studied the FRF process by developing an analytical model for predicting twisting web warping. The obtained results revealed that the longitudinal strain was inversely correlated with web warping. Woo et al. [16] investigated the shape defects in automotive parts produced by FRF. They concluded that the use of an FRF machine with a leveling roll would reduce longitudinal bow and edge wave defects. Ona et al. [17] examined the cause of web warping during FRF. They observed that the main cause of the phenomenon near a transition area was the occurrence of shrinkage during the forming of the area. Park et al. [18] investigated numerically and experimentally the defect of web warping. To reduce this defect, they proposed a new process called incremental counter forming (ICF). They controlled the longitudinal strain distribution on the profile flange by combination of forming and ICF parameters. They found that by increasing the longitudinal strain in convex and concave areas, the web warping defect can be reduced.

In previous studies that utilized optimization algorithms, efforts were made to achieve the optimal conditions for the

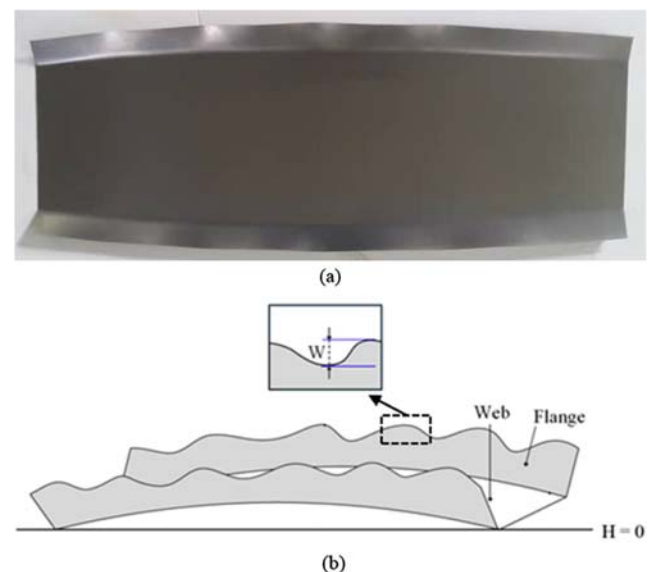


Fig. 3 Wrinkling caused by flexible roll forming process: **a** photograph and **b** schematic illustration

Table 1 Experiment plan

No.	Sheet thickness (mm)	Yield stress (MPa)	Blank shape
1	0.5	170	tr
2	0.5	170	cv
3	0.5	170	cc
4	0.5	404	tr
5	0.5	404	cv
6	0.5	404	cc
7	0.5	851	tr
8	0.5	851	cv
9	0.5	851	cc
10	0.8	170	tr
11	0.8	170	cv
12	0.8	170	cc
13	0.8	404	tr
14	0.8	404	cv
15	0.8	404	cc
16	0.8	851	tr
17	0.8	851	cv
18	0.8	851	cc
19	1.2	170	tr
20	1.2	170	cv
21	1.2	170	cc
22	1.2	404	tr
23	1.2	404	cv
24	1.2	404	cc
25	1.2	851	tr
26	1.2	851	cv
27	1.2	851	cc

fabrication of a product with minimal defects. Laouissi et al. [19] optimized the affected parameters of machining of gray cast iron using artificial neural networks (ANN), response surface methodology (RSM), and genetic algorithm (GA) methods. They showed the developed model for machining parameters using ANN and RSM is very useful tool for prediction propose, and the comparison of ANN with RSM showed that the prediction capacity of ANN method is more effective than the RSM

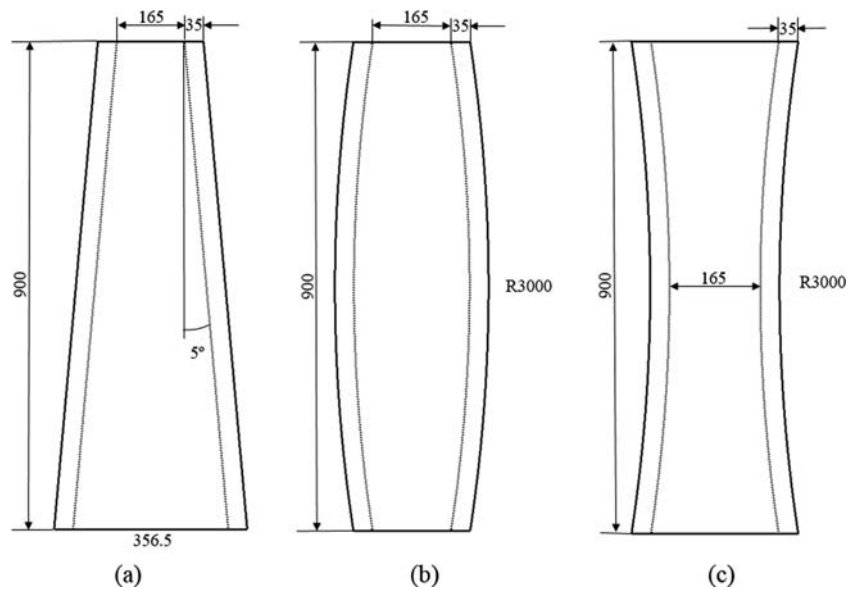
Table 2 Stress-strain values of three simulation materials

SPCC		SPFC 590		SPFC1180	
True strain	True stress (MPa)	True strain	True stress (MPa)	True strain	True stress (MPa)
0.00000	170.1475	0.00000	404.7290	0.00000	851.4797
0.06654	287.2302	0.03730	598.4652	0.01232	1129.111
0.12857	328.7990	0.07046	673.5364	0.02196	1240.612
0.19293	359.3925	0.10598	718.6440	0.03324	1291.614
0.26036	388.4670	0.14410	749.7615	0.04574	1317.026
0.33203	395.8192	0.18482	759.2974	0.05468	1321.600

approach. The optimal values of the machining parameters obtained from GA were close to the experimental results. Wiebenga et al. [20] controlled the occurrence of defects in the roll forming process using robust optimization. They showed that the scatter in the material properties is a significant factor in controlling the dimensional quality of the product.

They also showed that adjustment of the final rolls significantly improved the product quality by reducing the occurrence of defects and minimizing the destructive effects of scattered variables. Radovanovic [21] optimized the turning operation of AISI 1064 steel using three optimization approaches including Ip multi-media subsystem (IMS), multi-objective genetic algorithm (MOGA), and GA. Comparison of the three algorithm results with experiments showed that the IMS algorithm provides more appropriate solutions. Doriana et al. [22] optimized the hot forging process by combining of two methods of ANN and multi-objective optimization. They concluded that it was necessary to consider multiple processes when using global optimization methods to obtain optimal results. They also found that the simulation of tests using the finite element method could be replaced by the use of an artificial neural network (ANN), which is less sensitive to the problem dimensions compared with the design of experiment (DOE). Alizadeh and Omrani [23] integrated the robust multi-response Taguchi neural network with a CO₂ laser cutting process. They used the robust optimization to control the uncertainty of the neural network results. Bacanin and Tuba [24] and Yazdi et al. [25] presented a modification of the artificial bee colony (ABC) algorithm, referred to as genetically inspired artificial bee colony (GI-ABC). They showed that GI-ABC afforded an improvement on the performance of the ABC algorithm by applying uniform crossover and mutation operators obtained from GA. Yaghoobi et al. [26] optimized the pressure path in the hydroforming process using the neural fuzzy method and GA. They investigated the effect of the pressure path on the maximum thinning on the critical areas of the product by developing the adaptive neurofuzzy inference system (ANFIS) model based on simulation results and then the developed model is used as the objective function in the optimization process. High speed and avoiding trial and error and multiple simulations are the most important advantages of this method.

Fig. 4 Different blank geometries: a trapezoidal, b convex, and c concave (unit: mm)



As mentioned above, most previous studies on FRF focused on a general analysis of the process, the conditions under which defects occur, and the parameters that affect the defects. Because of the complexity of the process and the need to achieve products with minimal geometric defects, multi-objective optimization was combined with ANN in the present study. The shape defects were minimized by optimizing the parameters that affected them, thereby enabling the achievement of a product with the desired bend angle. Numerical simulation of the FRF was used to investigate the effect of the process parameters on two defects. The numerical results were verified by experiments performed using

a lab-scale FRF machine. The ANN was used to predict two defects as objective functions, and non-dominated sorting genetic algorithm II (NSGA-II) was subsequently used to optimize the input parameters for each target bend angle under the minimum conditions of the objective functions.

2 Finite element simulation

To investigate the longitudinal bow and wrinkling defects, FRF processes with and without leveling roll were simulated

Fig. 5 Flexible roll forming process: a schematic of the process simulation and b areas with different meshing densities

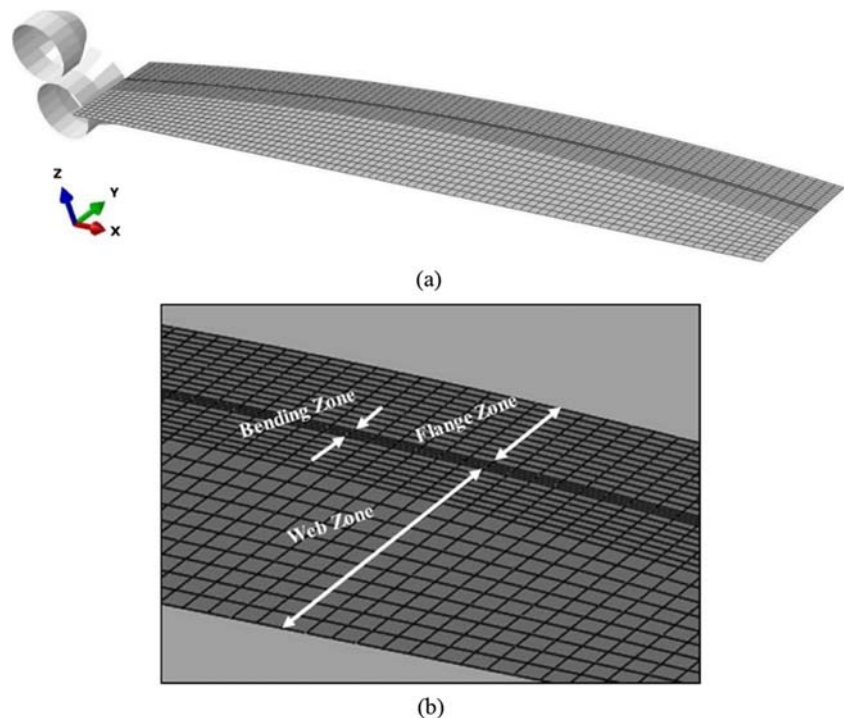


Table 3 Simulation conditions

Number of elements	2790
Size of elements	(1.5 to 10) × 4 mm
Element type	S4R
Integration points	7
Friction coefficient	0
Young's modulus	207 GPa
Poisson's ratio	0.3
Density	7850 kg/m ³

using the FEM code ABAQUS™ Implicit 6.14. The parameters that affect longitudinal bowing and wrinkling include the bend angle, sheet thickness, yield strength, and blank shape. Three blank shapes were considered in the analyses, namely, trapezoidal (tr), convex (cv), and concave (cc). To investigate the effects of the above parameters, an experiment was designed using the perfect factorial method. The experiment plan included 27 tests using target bend angles of 15–30° for two modes of FRF with and without leveling roll, which are 108 tests in total, as detailed in Table 1.

In the simulation, the sheets were modeled as shells and the rolls were considered to be rigid. A pair of forming rolls moved in the y -direction and rotated around the z -axis to shape an entire sheet. The results of the uniaxial tensile testing of the sheets were applied to the simulation. The stress and strain results are given in Table 2. An elastic-plastic material model and the von Mises yield criterion were employed, with the assumption of piecewise linear isotropic hardening.

For the simulation of the process, the rolls were considered as rigid body models, and the blank as a deformable part. Figure 4a-c show the geometries and dimensions of the three different blanks considered in this study.

The blank was modeled as a shell using type S4R shell elements. Figure 5a shows the simulated profiles, while Fig. 5b shows the blank meshing. Because of the greater deformation in the bending and flange zones, 1 mm × 3 mm meshing was applied to both, while larger meshing between

Table 4 Experimental conditions

Blank material	SPCC
Blank shape	Convex
Blank length, L	900 mm
Blank thickness	0.5 mm
Roll gap	0.5 mm
Web width, W	145 mm
Radius of blank, R	3000 mm
Flange width, F	15 mm, 25 mm, 35 mm
Bend angle	15°, 30°, 45°
Roll diameter	75 mm
velocity of feeding	0.26 m/min

**Fig. 6** Laboratory-scale FRF machine

1 mm × 3 mm and 9 mm × 3 mm was applied to the web zone. For definition of the contact condition between the blank and the rolls, the penalty approach was used.

The CPU time to complete the FE simulation was approximately 4 h. The Coulomb friction model was used, with the coefficient of friction considered to be 0 [27]. Table 3 summarizes the simulation conditions.

3 Experiments

To verify the numerical results, experiments were performed using SPCC blanks and the conditions detailed in Table 4. The laboratory-scale three-stand FRF machine shown in Fig. 6 was employed for the experiments.

The chemical composition and mechanical properties of SPCC, which is a type of aluminum, are summarized in Tables 5 and 6, respectively.

To confirm the FEM simulation results, the longitudinal strain at the flange edge was measured for three different conditions (flange width of 35 mm; sheet thickness of 2 mm; and bend angles of 15°, 30°, and 45°). The experiments shown in Fig. 7a-c were performed using the specifications in Table 4. The longitudinal strain during FRF was measured using a resistance strain gauges.

4 Optimization

In this study, the inputted effective parameters of the FRF process, such as the sheet thickness, yield strength, and blank shape, were optimally determined for each target bend angle. This was done to minimize the longitudinal bow and wrinkling, which were used as the two objective functions of the

Table 5 Chemical composition of SPCC (wt%)

Material	C	Mn	P	Si	Cr	Al
SPCC	0.19	0.58	0.04	0.15	0.11	0.003

Table 6 Mechanical properties of SPCC sheet

Material	Ultimate strength (MPa)	Yield stress (MPa)	Elongation (%)	Young's modulus (GPa)	Poisson's ratio	Density (kg/m ³)
SPCC	339	170	33.2	207	0.3	7850

ANN-based multi-objective optimization. The ANN was first used to find both objective functions, and Non-dominated Sorting Genetic Algorithm II was then used to optimize the input parameters to minimize the objective functions for each target bend angle.

4.1 Design of back-propagation neural network

An artificial neural network (ANN) is a parallel operating system that simulates the human neuron. Each neuron receives information from neurons in a previous layer and then distributes it to neurons in the next layer. As shown in Fig. 8, the neural network designed to find the objective functions (longitudinal bow and wrinkling) in this study has three layers, namely, the input, hidden, and output layers. Based on the number of inputs, the input layer has four units.

Under the condition that the issue determines the number of specific training patterns, the number of the hidden layer units can be specified by trial and error. To do this, a back-propagation neural network (BPNN) was developed in MATLAB. The network was tested using a number of hidden layer units between 3 and 40 and with 24 training patterns. Considering that the purpose of the network was to find two objective functions, the number of output layer units was considered to be 1. It was thus not necessary to assume the input

and output of the neural network. To accelerate the convergence of the network, different momentums and learning rates were used simultaneously. During the construction of the BPNN, many parameters had to be set. The initial learning rate was set to 0.001, while the number of hidden layer units was set to 1. Out of 108 data sets, 96 sets were selected as training data and 12 were used as test data. The effects of the number of hidden layer nodes, conversion function of the hidden layer, decrease and increase ratios of the training rate, and momentum on the quality of the network training were investigated. The training process was terminated when one of the two following convergence criteria was achieved:

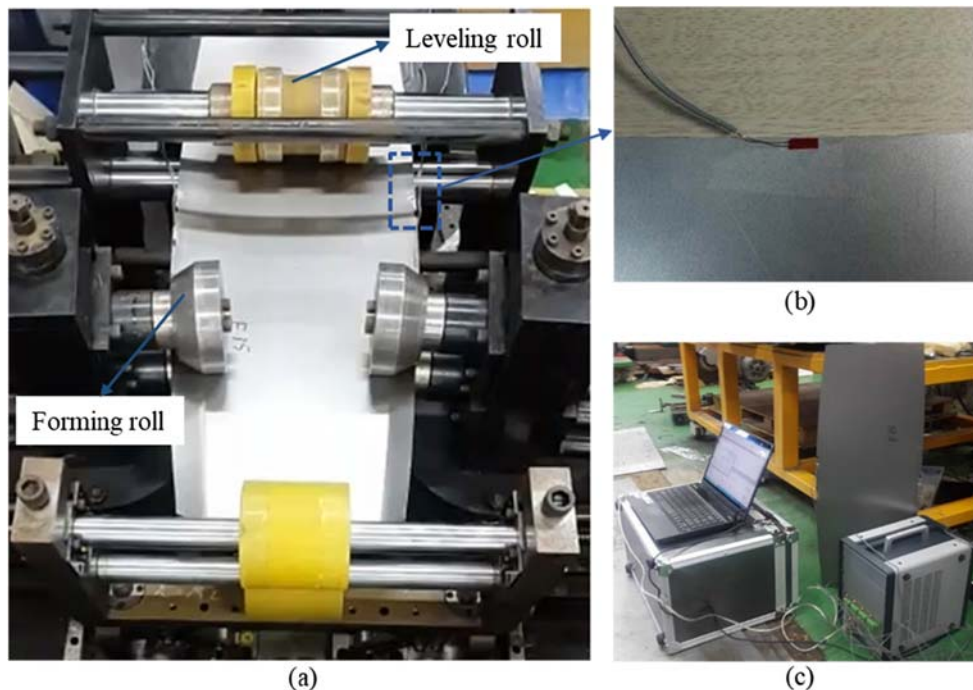
1. Mean squared error (MSE) < 0.001.
2. Number of repetitions = 50,000.

The quality of the training was specified by the mean squared error and the average mean squared error for all the repetitions, which are given by Eqs. 1 and 2, respectively.

$$MSE = \frac{1}{n} \sum_{j=1}^m \sum_{i=1}^n (T_{ij} - P_{ij})^2 \quad (1)$$

$$\overline{MSE} = \frac{1}{r} \sum_{q=1}^r MSE_q \quad (2)$$

Fig. 7 Measuring of the longitudinal strain by a strain gauge and data logger: **a** FRF experimental setup, **b** location of the strain gauge, and **c** data logger set



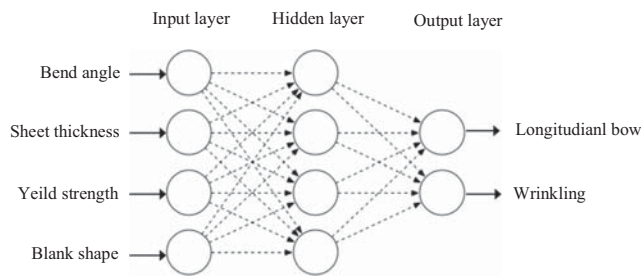


Fig. 8 Topology of the designed neural network

A simple and effective means of increasing and improving the learning rate to prevent instability and oscillation of the network is the addition of a momentum sentence to the Storm Descending (SD) algorithm. The idea of the back-propagation algorithm is the addition of an intersection or movement size to each parameter of the perceptron multi-layer network, so that the parameter tends to move in a direction that reduces the energy function.

4.2 Non-dominated sorting genetic algorithm for optimization

4.2.1 Definition of optimization

Objective optimization involves the optimization (i.e., minimization or maximization) of a single or several objectives using a number of inequality or equality constraints simultaneously [28]. The problem is described in detail as follows:

Find $x = (x_i) \forall i = 1, 2, \dots, N_{param}$ such that $f_i(x)$ is a minimum (or maximum) $\forall i = 1, 2, \dots, N_{obj}$.
subject to

$$g_j(x) = 0 \quad \forall j = 1, 2, \dots, M, \tag{3}$$

$$h_k(x) \leq 0 \quad \forall k = 1, 2, \dots, K, \tag{4}$$

where x is a vector include the N_{param} design parameters, $(f_i)_{i=1, \dots, N_{obj}}$ is the objective function, and N_{obj} is the number of objectives.

4.2.2 Non-dominated sorting and Pareto front

In this method, unlike single-objective optimization, there is no single optimal solution, but a set of solutions is created that none are dominate to the other, and this is called pareto optimal solutions.

Here, the constraint violation $\ell(X)$ of an individual X is defined as the sum of the violated constraint function values [29]:

$$\ell(X) = \sum_{j=1}^B \gamma(g_j(X))g_j(X) \tag{5}$$

where γ is the Heaviside step function. A set of non-dominated individuals is used to form a Pareto-optimal front [29].

4.2.3 Tournament selection

Each individual competes in exactly two tournaments with randomly selected individuals, a procedure that imitates the survival of the fittest in nature [28].

4.2.4 Controlled elitism sorting

To preserve diversity, the effect of elitism is controlled by using geometric distribution to choose the number of individuals from each subpopulation [29]:

$$S_q = S \frac{1-c}{1-c^w} c^{q-1} \tag{6}$$

To form a parent search population $P_t + 1$ (t denotes the generation) of size S , where $0 < c < 1$ and w is the total number of ranked non-dominated individuals.

4.2.5 Crowding distance

The crowding distance of each individual with its nearest neighbors is shown by this parameter. The crowding distance parameter is calculated for each member of the group and computes the density of the solutions around a specific point in the population. In fact, in order to calculate the density of solutions around a specific point in a population, the average distance between two points is taken from both sides and along each of the targets [29]. Hence, if the two individuals have the same rank, each one has a larger crowding distance than each other is better [30].

4.2.6 Crossover and mutation

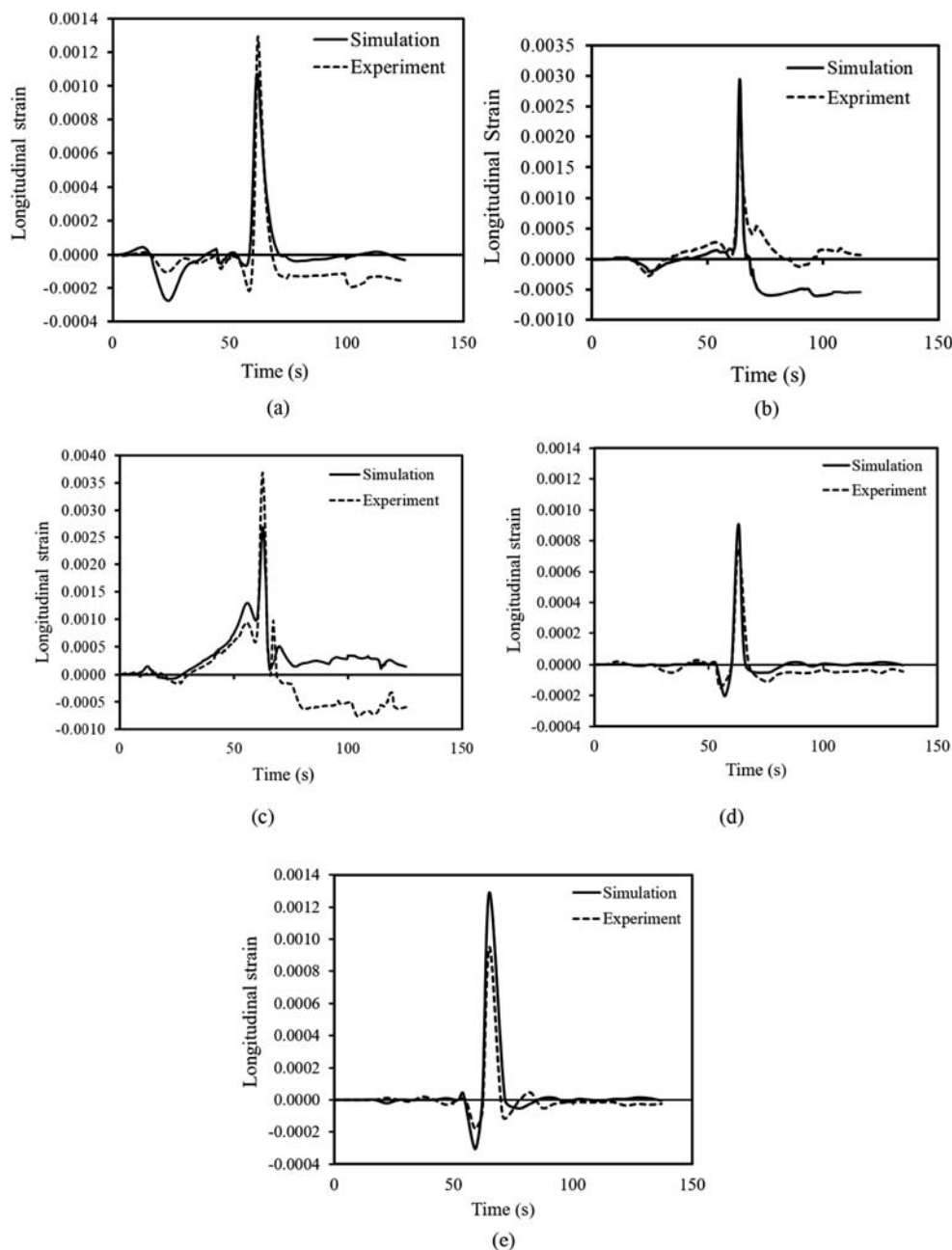
Uniform crossover and random uniform mutation were used to obtain the offspring population Q_{t+1} . The integer-based uniform crossover operator takes two distinct parent individuals and interchanges their corresponding binary bits with a probability $0 < p_c \leq 1$. After this crossover, the mutation operator also interchanges the binary bits with a mutation probability $0 < p_m < 0.5$ [28].

5 Results and discussion

5.1 Finite element model validation

Figure 9a-c compare the longitudinal strains determined by simulation and experiment. As can be observed from the figure, the maximum longitudinal strain occurs at the edge of the sheet, specifically near the forming stand, due to the elongation of the sheet before it reaches the forming stand. As can

Fig. 9 Comparison of longitudinal strains determined by simulation and experiment; a convex blank, a thickness of 0.5 mm, a flange width of 35 mm, and bend angles of **a** 15°, **b** 30°, and **c** 45° for SPCC and bend angle of 30° for **d** SPFC590 and **e** SPFC1180



also be observed, there is good agreement between the simulation and experimental results, confirming the accuracy of the model used for the simulation.

5.2 Effects of network structural parameters on training quality

5.2.1 Selection of initial weights and biases of layers

The first step in applying the error-back propagation algorithm is the determination of the initial weights

and biases of the layers. The use of appropriate values would enable faster convergence of the post-propagation algorithm. The initial values used for the present network were generated by the `init(net)` function, which randomly creates weights and initial biases. The effects of the activation functions of the hidden layer nodes on the network learning quality are given in Table 7.

Because the values of \overline{MSE} and MSE_{min} for the sigmoid function are less than those for the other two functions, the sigmoid function was selected as the hidden layer activity function.

Table 7 Effects of the activation functions of the hidden layer nodes

Test no.	Activation function	\overline{MSE}	MSE_{min}
12	Sigmoid	0.00752	0.004831
13	Hyperbolic tangent	0.0845	0.005941
14	Linear	0.2543	0.2261

Table 8 Effects of the momentum on the network training quality

Test no.	Momentum	\overline{MSE}	MSE_{min}
21	0.65	0.012107	0.008452
22	0.70	0.015410	0.004452
23	0.75	0.01659	0.006215
24	0.80	0.009132	0.007120
41	0.85	0.003903	0.003234

5.2.2 Momentum

The momentum allows the network to neglect the small-scale features at the error level. Table 8 gives the effects of the momentum on the network training quality.

The results show that the errors are minimum for a momentum of 0.85.

5.2.3 Performance of BPNN

The network performance significantly depends on the selection of the test couples. In this study, the number of performance tests was systematically increased. Each network performance test was performed using three sets of

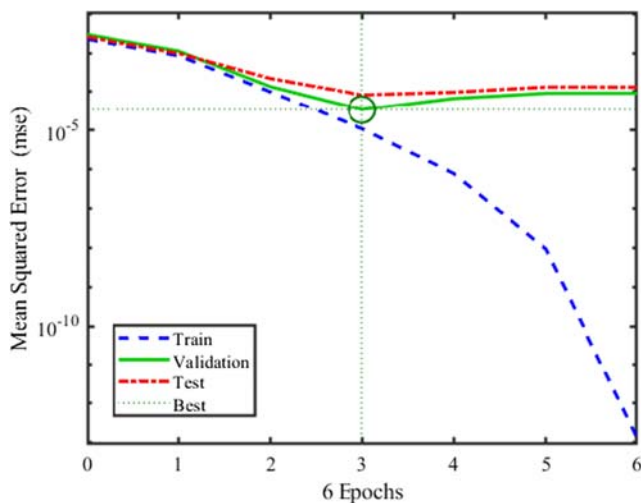


Fig. 10 Network error curve obtained from the performance test with the least MSE

data randomly selected from Table. 2. To evaluate the network performance, the mean squared error for each test was calculated, and the network corresponding to the training and test data sets that produced the lowest MSE was selected as the final network. Obviously, the weights and biases of the final network were related to the performance test that produced the least MSE . Figure 10 shows the network error curve obtained from the performance test that produced the least MSE .

A data set consists of 96 set for each output that were unseen by the ANN during training, and they were used to test the trained ANN. The qualitative accuracy spread of the training and test samples are shown in Fig. 11a-d. The points are clustered along the 45° line, indicating that the predicted values are close to the true values.

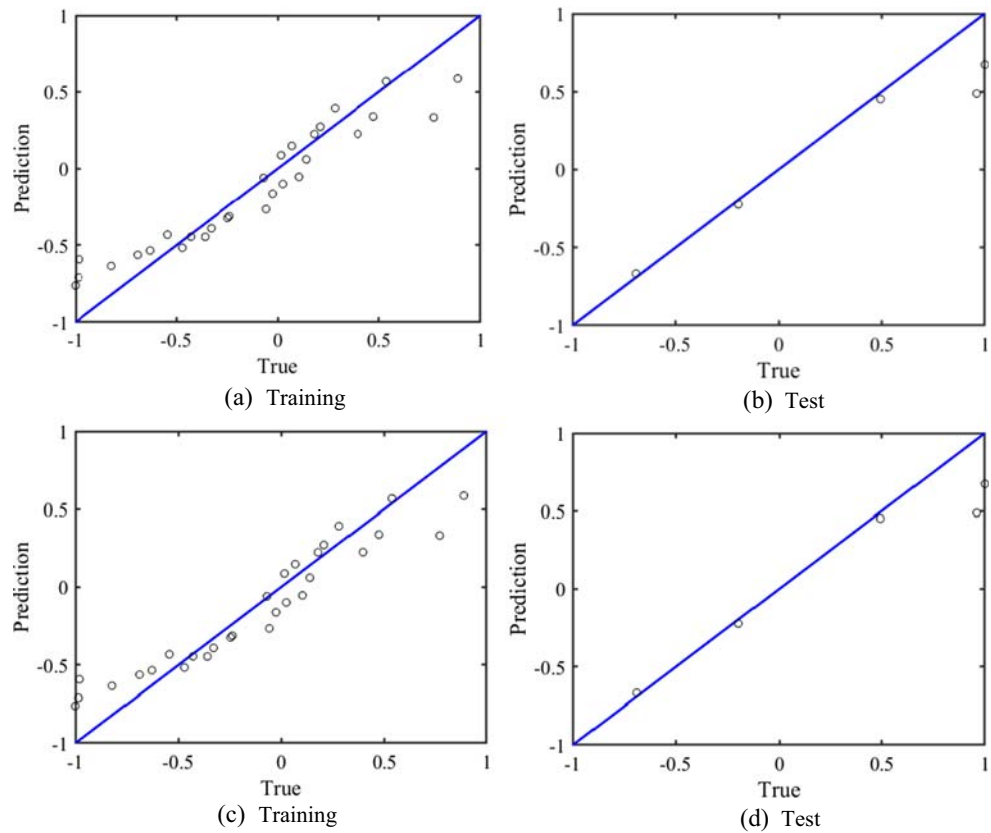
Table 9 compares the neural network training outputs and the desired outputs for the longitudinal bow and wrinkling. As can be observed, there is good agreement between the predictions of the neural network and the desired outputs.

5.3 Optimal values of design parameters for minimizing objective functions and minimum values of objective functions

In the present study, the objective functions were the longitudinal bow and wrinkling, which were to be minimized. Three design parameters, namely, the sheet thickness, yield strength, and blank shape, were considered for each target bend angle. The lower and upper bounds of these parameters are listed in Table 10.

Multi-objective optimization involves the simultaneous optimization of several fitness parameters. For this purpose, the Pareto front theory is used instead of single-objective optimization concepts, and the final solution is chosen from the

Fig. 11 Accuracy spread of the ANN predictions (prediction vs. true value): **a** training and **b** test longitudinal bow data and **c** training and **d** test wrinkling data



optimal Pareto front collection. A design vector x^* is a Pareto optimum if and only if there is no other feasible vector x such that [31]

$$f_i(x) \leq f_i(x^*) \quad (7)$$

$i = 1, 2, \dots, n$

and

$$f_j(x) < f_j(x^*) \text{ for at least one } j, 1 \leq j \leq n. \quad (8)$$

After the execution of the optimization algorithm, the Pareto optimal solutions were obtained for all the target bend angles. Figure 12a and b show the Pareto-optimal

Table 9 Comparison of the ANN training outputs with the desired outputs for longitudinal bow and wrinkling

Test no.	Longitudinal bow (mm) Desired output	Longitudinal bow (mm) Training output	Error (%)	Wrinkling (mm) Desired output	Wrinkling (mm) Training output	Error (%)
2 (15°) Leveling roll ON	0.68	0.71	4.22	1.95	1.89	3.17
6 (18°) Leveling roll OFF	0.31	0.32	3.12	0.45	0.43	4.65
10 (21°) Leveling roll ON	1.06	0.99	7.07	2.31	2.38	2.94
14 (24°) Leveling roll OFF	3.22	3.26	1.22	3.95	3.90	1.28
20 (30°) Leveling roll ON	9.00	8.84	1.80	4	4.24	5.6
24 (24°) Leveling roll OFF	4.19	4.31	2.78	0.70	0.72	2.77

Table 10 Decision variables and their ranges

Parameter	Lower bound	Upper bound
Sheet thickness (mm)	0.1	1.5
Yield strength (MPa)	170	900
Blank shape	1	3

curves obtained using NSGA-II for a target angle of 15° in FRF with and without leveling roll, respectively.

The best results were selected through ranked selection and identification of the optimal Pareto front for the decision variables and objective functions.

The optimal values of the design parameters and the obtained values of the objective functions of the longitudinal bow and wrinkling for different target bend angles in FRF with and without leveling roll are presented in Tables 11 and 12, respectively.

The distributions of the three design parameters considered for the optimization are presented with respect to the generation in Fig. 13a-c. From the distributions of all the parameters and their scattering over their allowable

variation ranges, it can be concluded that the sheet thickness has the greatest effect on the minimization of the two objective functions for all the target bend angles, followed by the yield strength and the blank shape, respectively.

After the optimization, the results were compared with those of the experiments and numerical simulations. Figure 14a-d compare the experimental, numerical, and optimization results of the longitudinal bow and wrinkling for FRF with and without leveling roll. Good agreement can be observed between the results.

6 Conclusion

In this study, ANN-based multi-objective optimization (NSGAI) was used to optimize the effective parameters of the FRF process, such as the sheet thickness, yield strength, and blank shape, with respect to the target bend angle, to minimize the longitudinal bow and wrinkling of the product. Following is a summary of the findings of the study and the conclusions drawn from it.

Fig. 12 Pareto-optimal curves obtained using NSGA-II for a target angle of 15° in FRF **a** with leveling roll and **b** without leveling roll

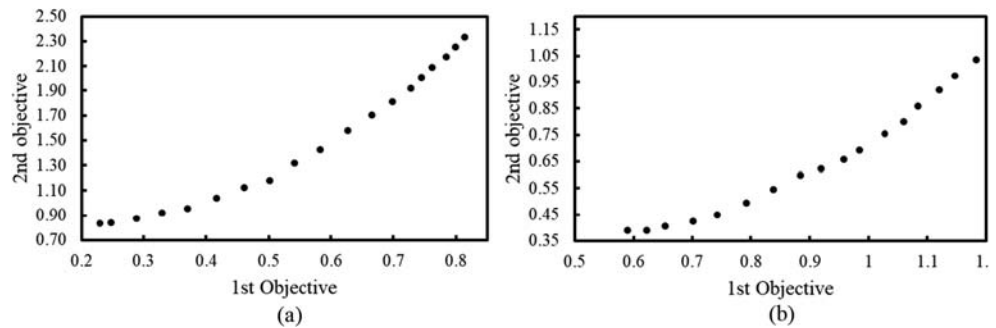


Table 11 Optimal values of the design parameters and the obtained values of the objective functions of the longitudinal bow and wrinkling for different target bend angles in FRF with leveling roll

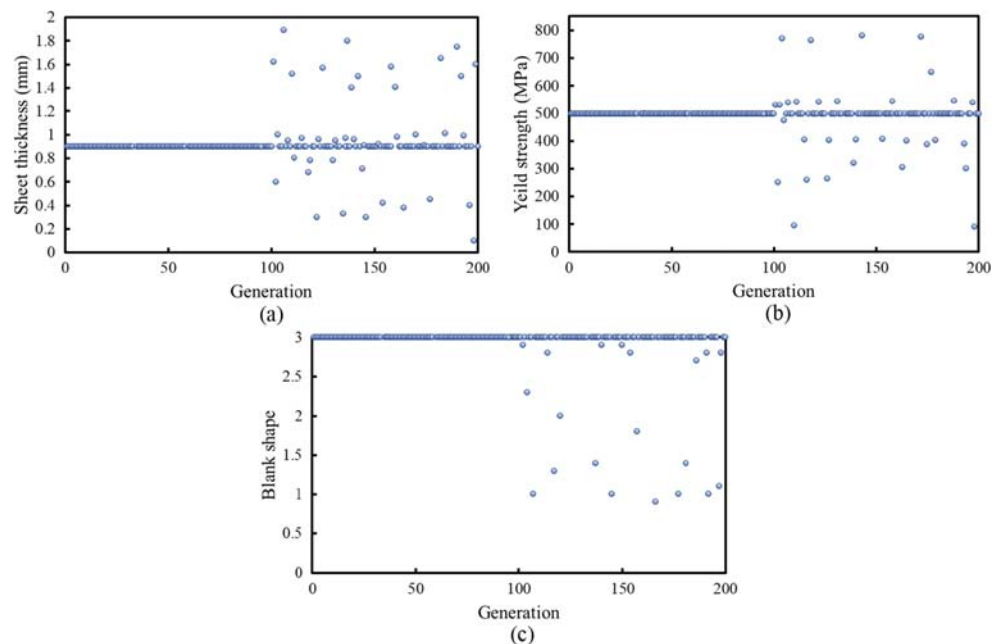
Row	Target bend angle (degree)	Thickness (mm)	Yield strength (MPa)	Blank shape	Longitudinal bow (mm)	Wrinkling (mm)
1	15	0.7	851	tr	0.23	0.84
2	16	0.4	785	cc	0.11	0.36
3	17	0.6	819	cc	0.28	0.57
4	18	0.3	851	cv	0.31	1.22
5	19	0.7	672	cc	0.45	1.30
6	20	0.8	350	cc	0.19	1.18
7	21	0.9	535	cc	0.41	0.95
8	22	0.5	297	tr	0.79	1.65
9	23	1	610	cc	0.29	0.98
10	24	0.9	498	cc	0.28	1.08
11	25	0.6	185	cc	0.31	2.72
12	26	0.7	440	tr	1.52	2.81
13	27	0.5	404	cc	0.39	2.02
14	28	0.5	851	cv	1.05	2.21
15	29	0.5	190	cc	1.15	1.79
16	30	0.8	404	cc	0.37	1.21

Table 12 Optimal values of the design parameters and the obtained values of the objective functions of the longitudinal bow and wrinkling for different target bend angles in FRF without leveling roll

Row	Target bend angle (degree)	Thickness (mm)	Yield strength (MPa)	Blank shape	Longitudinal bow (mm)	Wrinkling (mm)
1	15	0.9	851	cc	0.59	0.39
2	16	0.6	650	cc	0.32	0.36
3	17	0.7	570	cc	0.65	0.41
4	18	0.5	452	cc	0.30	0.44
5	19	0.8	851	tr	0.61	0.76
6	20	0.5	385	cc	0.35	1.02
7	21	1	450	cc	0.81	0.66
8	22	0.6	425	cc	0.37	0.58
9	23	0.9	215	tr	1.17	1.03
10	24	0.5	625	cv	2.10	1.81
11	25	0.7	305	cc	0.75	1.17
12	26	0.8	380	tr	2.4	1.51
13	27	1	404	cc	0.86	0.92
14	28	0.6	190	tr	3.38	1.97
15	29	0.6	214	cc	1.25	1.48
16	30	0.8	851	cc	0.97	0.99

- 1) Because the neural network is based more on statistics than a physical model, it is suitable for modeling the multi-parameter FRF process. The BPNN training algorithm was thus used to predict the two defects as the objective functions.
- 2) To increase the learning rate of the conventional BPNN and prevent instability and oscillation of the network, a momentum sentence was added to the Storm Descending (SD) algorithm.
- 3) Among the activation functions of the hidden layer nodes, the sigmoid function was selected as the function of the hidden layer nodes owing to its lower \overline{MSE} and MSE_{\min} values.
- 4) The network prediction capabilities were confirmed by network prediction error analysis, and the BP network prediction results were found to be in good agreement with those of numerical simulation.
- 5) In the use of NSGAI1 to optimize the input parameters for minimization of the objective functions with respect to the target bend angle, the best results were chosen from the optimal Pareto front collection. The choice was based on ranked selection, the optimal

Fig. 13 Distributions of the design parameters with respect to their population index: **a** sheet thickness, **b** yield strength, and **c** blank shape



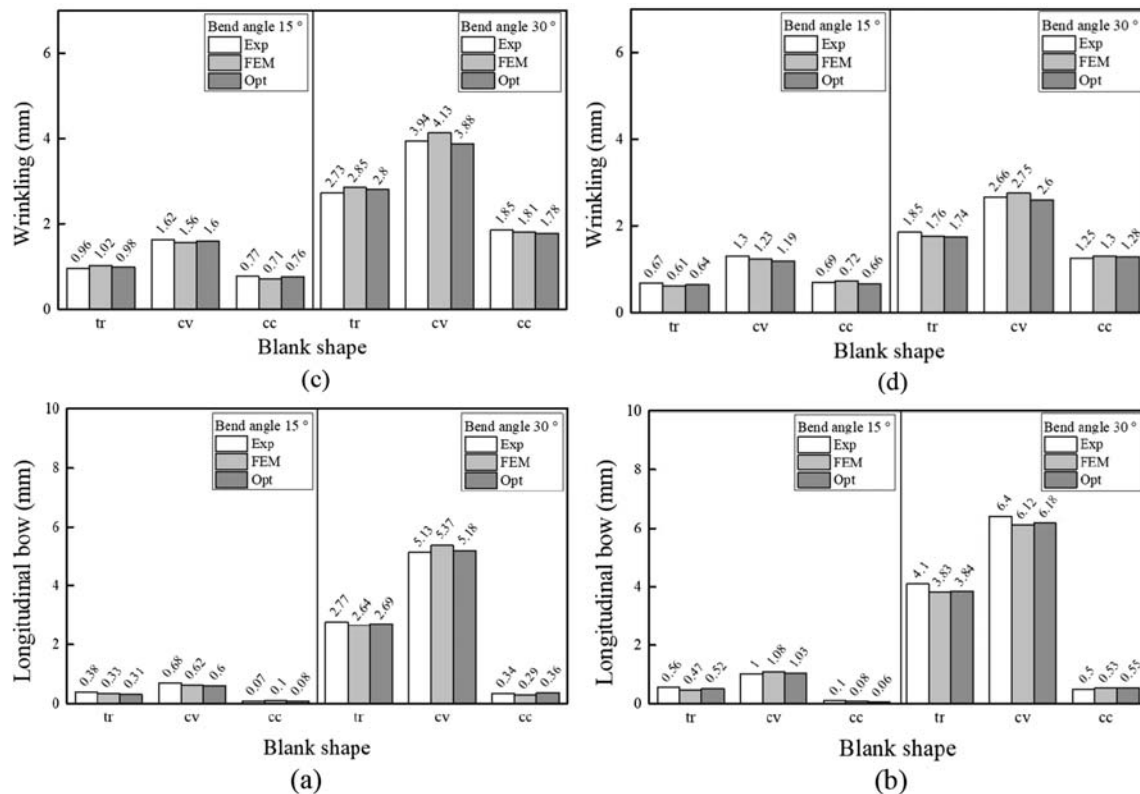


Fig. 14 Comparison of the experimental, numerical simulation, and optimization results of the longitudinal bow **a** with leveling roll, **b** without leveling roll and wrinkling, **c** with leveling roll, and **d** without leveling roll

values of the design parameters, and the minimum values of the objective functions of the longitudinal bow and wrinkling for FRF with and without leveling roll.

- 6) The distributions of all the parameters and their scattering over their allowable variation ranges showed that the sheet thickness had the greatest effect on the minimization of the two objective functions, followed by the yield strength and blank shape, respectively.

Funding information This work was supported by the National Research Foundation of Korea (NRF) grant funded by the Korea government (MSIT) (No. 2019R1A5A6099595)

References

- Sweeney K, Grunewald U (2003) The application of roll forming for automotive structural parts. *J Mater Process Technol* 132(1–3): 9–15. [https://doi.org/10.1016/S0924-0136\(02\)00193-0](https://doi.org/10.1016/S0924-0136(02)00193-0)
- Kim SY, Joo BD, Shin S, Van Tyne CJ, Moon YH (2013) Discrete layer hydroforming of three-layered tubes. *Int J Mach Tool Manu* 68(1):56–62. <https://doi.org/10.1016/j.ijmactools.2013.02.002>
- Yan Y, Wang H, Li Q, Qian B, Mpofu K (2014) Simulation and experimental verification of flexible roll forming of steel sheets. *Int J Adv Manuf Technol* 72(1–4):209–220. <https://doi.org/10.1007/s00170-014-5667-0>
- Jeon CH, Han SW, Joo BD, Van Tyne CJ, Moon YH (2013) Deformation analysis for cold rolling of Al-Cu double layered sheet by the physical modeling and finite element method. *Met Mater Int* 19(5):1069–1076. <https://doi.org/10.1007/s12540-013-5023-1>
- Han SW, Woo YY, Hwang TW, Oh IY, Moon YH (2018) Tailor layered tube hydroforming for fabricating tubular parts with dissimilar thickness. *Int J Mach Tool Manu* 138:51–65. <https://doi.org/10.1016/j.ijmactools.2018.11.005>
- Dadgar Asl Y, Sheikhi M, Pourkamali Anaraki A, Panahizadeh Rahimloo V, Hosseinpour Gollo M (2017) Fracture analysis on flexible roll forming process of anisotropic Al6061 using ductile fracture criteria and FLD. *Int J Adv Manuf Technol* 91(5–8):1481–1492. <https://doi.org/10.1007/s00170-016-9852-1>
- Qiu N, Li M, Li R (2016) The shape analysis of three-dimensional flexible rolling method. *Proc Inst Mech Eng B J Eng Manuf* 230(4): 618–628. <https://doi.org/10.1177/0954405414566056>
- Woo YY, Han SH, Hwang TW, Park JY, Moon YH (2018a) Characterization of the longitudinal bow during flexible roll forming of steel sheets. *J Mater Process Technol* 252:82–794. <https://doi.org/10.1016/j.jmatprotec.2017.10.048>
- Kasaei MM, MoslemiNaeni H, Abbaszadeh B, Mohammadi M, Ghodsi M, Kiuchi M, Zolghadr R, Liaghat Gh, AziziTafti R, Salmani Tehrani M (2014) Flange wrinkling in flexible roll forming process, 11th International Conference on Technology of Plasticity, ICTP 2014, 19–24 October
- Farzin M, Salmani Tehrani M, Shameli E (2002) Determination of buckling limit of strain in cold roll forming by the finite element analysis. *J Mater Process Technol* 125–126:26–32. [https://doi.org/10.1016/S0924-0136\(02\)00357-6](https://doi.org/10.1016/S0924-0136(02)00357-6)
- Salmani Tehrani M, Hartley P, Moslemi Naeni H, Khademzadeh H (2006) Determination of buckling limit of strain in cold roll forming by the finite element analysis. *Tin Wall Struct* 44:184–196. [https://doi.org/10.1016/S0924-0136\(02\)00357-6](https://doi.org/10.1016/S0924-0136(02)00357-6)

12. Gulceken E, Abeé A, Sedlmaier A, Livatyali H (2007) Finite element simulation of flexible roll forming, a case study on variable width U channel. 4th International Conference and Exhibition on Design and Production of Machines and Dies/Molds, Cesme, Turkey, Jun 21–23
13. Larrinaga J, Galdos L (2009) Geometrical accuracy improvement of flexibly roll formed profiles by means of local heating. First International Congress on Roll Forming, Bilbao
14. Mohammadi M, MoslemiNaeini H, Kasaei MM, Salmani Tehrani M, Abbaszadeh B (2014) Investigation of web warping of profiles with changing cross section inflexible roll forming process. *Modares Mech Eng* 14(6):72–80 (in Persian)
15. Jiao J, Rolfe B, Mendiguren J, Weiss M (2015) An analytical approach to predict web-warping and longitudinal strain in flexible roll formed sections of variable width. *Int J Mech Sci* 90:228–238. <https://doi.org/10.1016/j.ijmecsci.2014.11.010>
16. Woo YY, Han SH, Oh IY, Moon YH (2018b) Shape defects in the flexible roll forming of automotive parts. *Int J Automot Technol* 20(2):227–236. <https://doi.org/10.1007/s12239-019-0022-y>
17. Ona H, Shou I, Hoshi K (2012) On strain distributions in the formation of flexible channel section development of flexible cold roll forming machine. *Int J Mater Res* 576:137–140. <https://doi.org/10.4028/www.scientific.net/AMR.576.137>
18. Park JC, Yang DY, Cha MH, Kim DG, Namb GB (2014) Investigation of a new incremental counter forming in flexible roll forming to manufacture accurate profiles with variable cross sections. *Int J Mach Tool Manu*:68–80. <https://doi.org/10.1016/j.ijmachtools.2014.07.001>
19. Aissa Laouissi A, Yaltese MA, Belbah A, Belhadi S, Haddad (2019) Investigation, modeling, and optimization of cutting parameters in turning of gray cast iron using coated and uncoated silicon nitride ceramic tools. Based on ANN, RSM, and GA optimization. *Int J Adv Manuf Technol* 101:523–548. <https://doi.org/10.1007/s00170-018-2931-8>
20. Wiebenga JH, Weissb M, Rolfec B, van den Boogaard AH (2013) Product defect compensation by robust optimization of a cold roll forming process. *J Mater Process Technol* 213:978–986. <https://doi.org/10.1016/j.jmatprotec.2013.01.006>
21. Radovanovic M (2019) Multi-objective optimization of multi-pass turning AISI 1064 steel. *Int J Adv Manuf Technol* 100:87–100. <https://doi.org/10.1016/j.jmatprotec.2013.01.006>
22. Doriana MD’ Addona, Dario Antonelli (2018) Neural network multi objective optimization of hot forging. 11th CIRP Conference on Intelligent Computation in Manufacturing Engineering, 19–21 July, Ischia, Italy, *Procedia CIRP* 67:498–503
23. Alizadeh A, Omrani H (2019) An integrated multi response Taguchi- neural network- robust data envelopment analysis model for CO2 laser cutting. *Measurement* 131:69–78. <https://doi.org/10.1016/j.measurement.2018.08.054>
24. Bacanin N, Tuba M (2012) Artificial bee colony (ABC) algorithm for constrained optimization improved with genetic operators. *Stud Inform Control* 21(2):137–146. <https://doi.org/10.24846/v21i2y201203>
25. Yazdi M, Latifi Rostami S, Kolahdooz A (2016) Optimization of geometrical parameters in a specific composite lattice structure using neural networks and ABC algorithm. *J Mech Sci Technol* 30(4):1763–1771. <https://doi.org/10.1007/s12206-016-0332-1>
26. Yaghoobi A, Bakhshi-Jooybari M, Gorji A, Baseri H (2016) Application of adaptive neuro fuzzy inference system and genetic algorithm for pressure path optimization in sheet hydroforming process. *Int J Adv Manuf Technol* 86(9–12):2667–2677. <https://doi.org/10.1007/s00170-016-8349-2>
27. Bui QV, Ponthot JP (2008) Numerical simulation of cold roll-forming processes. *J Mater Process Technol* 202(1–3):275–282. <https://doi.org/10.1016/j.jmatprotec.2007.08.073>
28. Hajabdollahi Z, Hajabdollahi F, Mahdi T, Hajabdollahi H (2013) Thermo-economic environmental optimization of Organic Rankine Cycle for diesel waste heat recovery. *Energy* 63:142–151. <https://doi.org/10.1016/j.energy.2013.10.046>
29. Deb K (2001) Multi-objective optimization using evolutionary algorithms. John Wiley & Sons, Hoboken
30. Deb K, Goel T (2001) Controlled elitist non-dominated sorting genetic algorithms for better convergence. In: Proceedings of the first international conference on evolutionary multi-criterion optimization Zurich 67–81
31. Kasprzak EM, Lewis KE (2001) Pareto analysis in multi objective optimization using the collinearity theorem and scaling method. *Struct Multidiscip Optim* 22:208–218. <https://doi.org/10.1007/s001580100138>

Publisher’s note Springer Nature remains neutral with regard to jurisdictional claims in published maps and institutional affiliations.